The Astrophysical Journal, 784:89 (14pp), 2014 April 1 doi:10.1088/0004-637X/784/2/89

LOW ENERGY NEUTRAL ATOMS FROM THE HELIOSHEATH

S. A. Fuselier[1,2], F. Allegrini[1,2], M. Bzowski[3], M. A. Dayeh[1], M. Desai[1,2], H. O. Funsten[4], A. Galli[5], D. Heirtzler[6], P. Janzen[7], M. A. Kubiak[3], H. Kucharek[6], W. Lewis[1], G. Livadiotis[1], D. J. McComas[1,2], E. Möbius[6], S. M. Petrinec[8], M. Quinn[6], N. Schwadron[6], J. M. Sokół[3], K. J. Trattner[8,10], B. E. Wood[9], and P. Wurz[5]

[1] Southwest Research Institute, San Antonio, TX 78228, USA; sfuselier@swri.edu, fallegrini@swri.edu, maldayeh@swri.org, mdesai@swri.edu, wlewis@swri.edu, george.livadiotis@swri.org, dmccomas@swri.edu

[2] University of Texas, San Antonio, TX 78249, USA; sfuselier@swri.edu, fallegrini@swri.edu, dmccomas@swri.edu

[3] Space Research Centre of the Polish Academy of Sciences, Bartycka 18A, 00-716 Warsaw, Poland; bzowski@cbk.waw.pl, jsokol@cbk.waw.pl, mkubiak@cbk.waw.pl

[4] Los Alamos National Laboratory, Los Alamos, NM 87545, USA; hfunsten@lanl.gov

[5] Physikalisches Institut, University of Bern, 3012 Bern, Switzerland; andre.galli@space.unibe.ch; peter.wurz@space.unibe.ch

[6] University of New Hampshire, Durham, NH 03824, USA; dheirtzl@atlas.sr.unh.edu, harald.kucharek@unh.edu, eberhard.moebius@unh.edu, n.schwadron@unh.edu, marty@drsri.com

[7] University of Montana, Missoula, MT 59812, USA; paul.janzen@umontana.edu

[8] Lockheed Martin Advanced Technology Center, Palo Alto, CA 94304, USA; steven.m.petrinec@lmco.com, karlheinz.trattner@lasp.colorado.edu

[9] Naval Research Laboratory, Washington, DC 20375, USA; brian.wood@nrl.navy.mil

Received 2013 November 12; accepted 2014 February 1; published 2014 March 7

ABSTRACT

In the heliosheath beyond the termination shock, low energy (<0.5 keV) neutral atoms are created by charge exchange with interstellar neutrals. Detecting these neutrals from Earth's orbit is difficult because their flux is reduced substantially by ionization losses as they propagate from about 100 to 1 AU and because there are a variety of other signals and backgrounds that compete with this weak signal. Observations from *IBEX-Lo* and *-Hi* from two opposing vantage points in Earth's orbit established a lower energy limit of about 0.1 keV on measurements of energetic neutral atoms (ENAs) from the heliosphere and the form of the energy spectrum from about 0.1 to 6 keV in two directions in the sky. Below 0.1 keV, the detailed ENA spectrum is not known, and *IBEX* provides only upper limits on the fluxes. However, using some assumptions and taking constraints on the spectrum into account, we find indications that the spectrum turns over at an energy between 0.1 and 0.2 keV.

Key words: ISM: atoms – plasmas – solar wind – Sun: heliosphere

Online-only material: color figures

1. INTRODUCTION

The *IBEX* mission was launched in 2008 in Earth's orbit to discover the global interaction of the heliosphere with the interstellar medium (McComas et al. 2009a). *IBEX* has two energetic neutral atom (ENA) cameras with ∼7° FWHM fields of view (FOV) that image neutral atoms in two overlapping energy ranges. *IBEX-Lo* images energetic neutral atoms (ENAs) in eight broad energy channels from 0.01 to 2 keV (Fuselier et al. 2009a) and *IBEX-Hi* images ENAs in six broad energy channels from 0.3 to 6 keV (Funsten et al. 2009a). The two cameras view perpendicular to the spin axis, and this axis points nearly in the Sun direction. By repointing the spin axis toward the Sun periodically (every orbit and, since 2011 June, every half orbit; McComas 2012), a set of maps (one for each energy channel) covering the entire sky is produced every 6 months. Thus, except for the ecliptic poles, the revisit time for any given region in the sky is 6 months.

Energetic neutral hydrogen atoms are produced in the outer heliosphere and heliosheath when protons (e.g., from the solar wind and embedded pickup protons) charge exchange with interstellar neutrals entering the heliosphere. To detect heliospheric neutrals at Earth's orbit, the velocity vector of the parent ion must be directed back into the inner solar system. Figure 1 is a schematic that illustrates the charge exchange (CX) processes in the heliosphere and inner and outer heliosheath that produce hydrogen ENAs that can be detected by *IBEX*. From top to bottom, there are four direct processes involving one or two charge exchange events and an additional process that involves three charge exchange events. The processes are organized by energy, but there is significant energy overlap for the ENA populations resulting from any of the individual processes.

The solar wind ion distribution is decelerated across the termination shock (TS; Richardson et al. 2008) (process 1 in Figure 1), and some ions in this distribution charge exchange with interstellar neutral atoms in the inner heliosheath between the TS and the heliopause. The resulting ENAs (Gruntman et al. 2001) may contribute to the lowest energy population observable by *IBEX*. Some fraction of the pickup ion distribution created by charge exchange in the inner heliosheath may undergo a second charge exchange (process 2 in Figure 1), also creating a low energy ENA population (Malama et al. 2006). The pickup ion distribution created in the upstream solar wind (process 3a in Figure 1) is also decelerated and heated across the termination shock. Some of these pickup ions charge exchange in the inner heliosheath, creating a population of ENAs with energy that is higher than energies of populations created in processes 1 and 2 in Figure 1 (Malama et al. 2006). Finally, the highest energy ENAs (process 4 in Figure 1) are produced by solar wind (and pickup ions) that are accelerated at the termination shock and by turbulence in the inner heliosheath before charge exchanging in the inner heliosheath (Chalov & Fahr 2000; Chalov et al. 2003; Fahr et al. 2011; Siewert et al. 2012; Kucharek et al. 2013). The energy of these ENAs extends well beyond the 6 keV upper limit of the *IBEX* ENA cameras.

[10] Now at: University of Colorado, Boulder, CO 80303, USA.

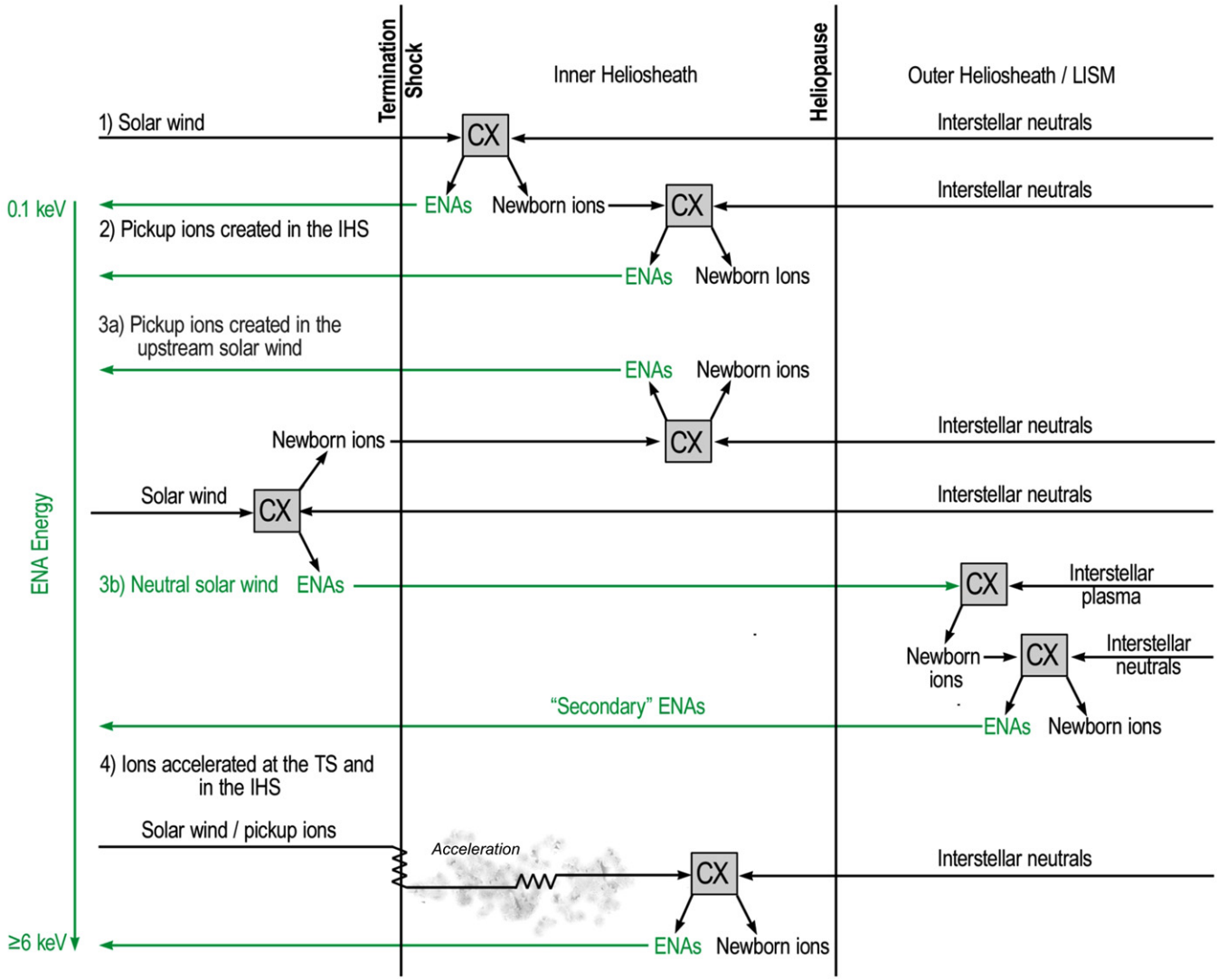

Figure 1. Schematic of the charge exchange processes in the outer heliosphere and inner and outer heliosheath that produce ENAs the *IBEX* observes. The processes are ordered by energy, but there is significant energy overlap for the neutrals produced in each individual process. ENAs are created by charge exchange (CX) of ions with interstellar neutrals, and these neutrals retain their velocity vector. When the velocity vector is directed back into the inner solar system, ENA imagers such as the ones on *IBEX* can detect them.

(A color version of this figure is available in the online journal.)

In addition to these single and double charge-exchange processes, a triple charge-exchange process (process 3b in Figure 1) creates neutrals from the parent solar wind ion population. An ion in the supersonic solar wind or in the inner heliosheath exchanges charge with a neutral, creating a fast neutral that escapes the heliosphere. This neutral exchanges charge a second time beyond the heliopause, creating a pickup ion in the nearby interstellar medium. The pickup ion exchanges charge a third time, creating a neutral atom that returns to the inner solar system (Izmodenov et al. 2009; Chalov et al. 2010; Heerikhuisen et al. 2010). Process 3b in Figure 1 is shown for a solar wind ion in the heliosphere. However, the initial charge exchange that starts this process can occur in the heliosphere or in the inner heliosheath and can occur between solar wind ions and interstellar neutrals or between pick up ions and interstellar neutrals (thus making it a quadruple charge-exchange process).

This "secondary ENA" process has been proposed as a mechanism to create the *IBEX* ribbon (McComas et al. 2009b; Chalov et al. 2010; Heerikhuisen et al. 2010; Schwadron & McComas 2013; Möbius et al. 2013) and may be an important mechanism for creating low energy neutrals observed from other directions in the sky as well (Desai et al. 2014; Heerikhuisen et al. 2013). Additional discussion of the secondary ENA process and other ENA populations is found in Izmodenov et al. (2009) and Chalov et al. (2010). For a recent review of processes that may create the *IBEX* ribbon, see McComas et al. (2014).

Initially, ENA fluxes observed by *IBEX* from ∼1 to 6 keV were not in good agreement with predictions from heliosphere/interstellar medium (ISM) models (Schwadron et al. 2009). However, fluxes in this energy range from ∼1 to 6 keV from most regions of the sky (excluding the *IBEX* Ribbon) are in relatively good agreement with results from the latest heliosphere/ISM models (Desai et al. 2014; Zank et al. 2010), and there is general agreement on how these ENAs are produced. *IBEX* observes a power law or a Kappa distribution over this energy range with a power law index of ∼−1.5 to −3 (Funsten et al. 2009b; McComas et al. 2009b). The extension of this power law to

energies less than 0.5 keV is more difficult to explain on the basis of bulk flow observations in the inner heliosheath (Fuselier et al. 2012). Although the plasma in the inner heliosheath is slowed and heated across the termination shock, on average, it is still moving away from the Sun with average radial bulk velocity of ~100 km s^{-1} (Richardson & Wang 2011). Accounting for the reported ENA fluxes below 0.5 keV requires high ion densities in the heliosheath (~0.1 cm^{-3}) and significant slowing and diversion of the bulk ion flow (Livadiotis et al. 2011, 2013), high plasma turbulence in the heliosheath (Gloeckler & Fisk 2010), another source of low energy neutrals from outside the heliosheath (Desai et al. 2014; Heerikhuisen, et al. 2013), some combination of these possibilities, or another yet unspecified source.

Since the ENA signal observed at 1 AU is very weak and the ENA detection techniques are susceptible to several backgrounds (Wurz et al. 2009), it is critical to determine the signal level, account for uncertainties in this level, and determine if there is a minimum energy below which background dominates. The *IBEX* mission design provides several important methods for distinguishing between near-Earth generated backgrounds (either ion or neutral) and the ENA signal from the outer heliosphere. Here three methods are highlighted.

The first method for distinguishing backgrounds from the ENA signal takes advantage of the fact that backgrounds may vary over an *IBEX* orbit, whereas the heliospheric ENA signal should not. In each orbit (initially ~7 days and, since 2011 June, ~9 days), the *IBEX* ENA cameras observe the same 360° × ~7° swath of the sky. The ENA signal should and does vary with look direction within the 360° × ~7° swath. However, in any given look direction, ENA fluxes from the outer heliosphere observed in the *IBEX* energy range are an integral line of sight accumulation over neutrals from tens of astronomical units (AU), at the very least. These fluxes should not exhibit large variations on timescales shorter than roughly several months (e.g., McComas et al. 2010). In contrast, a local, near-Earth background can have large variations over any timescale, including those shorter than an *IBEX* orbit. For example, ions accelerated at Earth's bow shock enter the *IBEX-Lo* sensor and create a background and are present intermittently over a wide range of timescales from minutes to hours (e.g., Fuselier et al. 2012). Short time variable backgrounds such as the example presented here are removed from the *IBEX* heliospheric ENA data set by using only those intervals when the flux is the lowest during a given orbit (McComas et al. 2012b). Although these *IBEX-Hi* and *-Lo* data culls differ for the two sensors (Fuselier et al. 2012), the selection of the lowest fluxes during a given orbit is a very efficient method for removing background that varies on timescales of less than about one week.

The second method that the *IBEX* mission design provides for distinguishing background and signal takes advantage of the fact that the two sensors have overlapping energy ranges. The *IBEX-Hi* and *-Lo* energy ranges overlap from 0.5 to 2 keV, with the lowest three energy channels of *IBEX-Hi* overlapping the highest three energy channels of *IBEX-Lo*. The two sensors have different detection techniques. Both convert ENAs to ions and then analyze the ion signal, but *IBEX-Hi* uses a carbon foil to strip the neutral atom of an electron, creating a positive ion (Funsten et al. 2009a), and *IBEX-Lo* uses a conversion surface to create a negative ion (Fuselier et al. 2009b). The two sensors also use different charged particle suppression techniques and are susceptible to different backgrounds. However, they were cross-calibrated in the laboratory prior to launch. Therefore, measurement of the same flux over their common energy range (e.g., McComas et al. 2009b; Fuselier et al. 2012) and observations of the same features (such as the ribbon) in the sky maps (McComas et al. 2012b) are powerful evidence for detection of heliospheric ENAs without significant interference from near-Earth backgrounds, at least for ribbon-level fluxes near 1 keV.

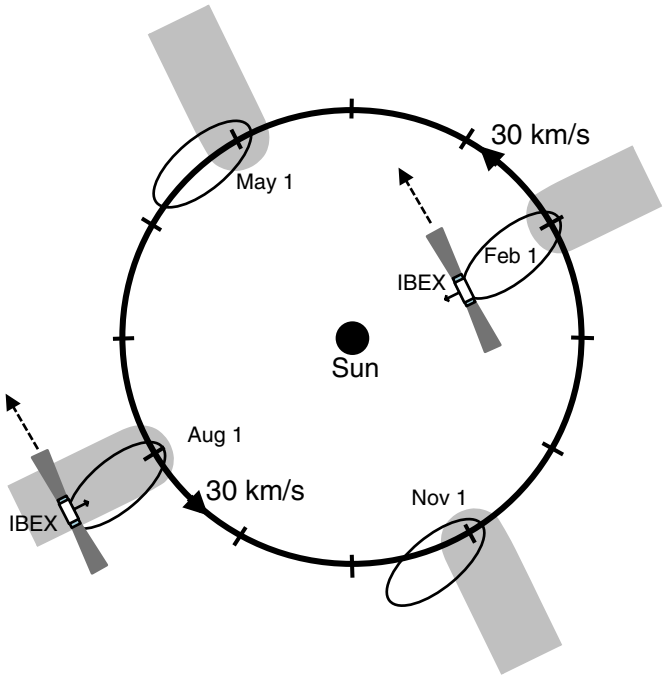

Figure 2. *IBEX*'s orbit around the Sun (not to scale). The spin axis is always directed within about 7° of the Sun, so that the sensors sample the same region of the sky every 6 months. The dashed lines show the view direction in the ecliptic in February and August. In February (August), heliospheric ENAs have the 30 km s^{-1} velocity of the Earth added to (subtracted from) them. ENA signal from the heliosphere should be the same in February and August, after the appropriate frame transformation. However, the ENA measurements in February and August are made in very different near-Earth regions and susceptible to different backgrounds. In February (August), ENA measurements are made when the spacecraft is in the solar wind (in Earth's magnetosphere, shown by the shaded regions).

The third method that the *IBEX* mission design provides for distinguishing background and signal takes advantage of the fact that measurement of fluxes from the same region of the sky at six-month intervals should agree with one another. The implicit assumption in this method is that the temporal variations in the ENA flux are small over 6 months (or even 18 months). However, this assumption is supported by observations over several years (McComas et al. 2010, 2012b; Reisenfeld et al. 2012) that show an overall decrease of the order of 15% in fluxes at energies near 1 keV in many directions in the sky, including those that are considered in this paper.

Figure 2 illustrates this third method, showing the orbit of the *IBEX* spacecraft and the fields-of-view of the *IBEX* sensors projected into the ecliptic plane. The spacecraft spin axis is maintained close to the Sun direction throughout the year. Therefore, the *IBEX* sensors revisit the same region of the sky every 6 months, except at the ecliptic poles. For example, *IBEX* sensors sample the region of the sky in the ecliptic toward the upper-left corner of Figure 2 in February–March and August–September every year. Since *IBEX* orbits the Earth, neutrals from this

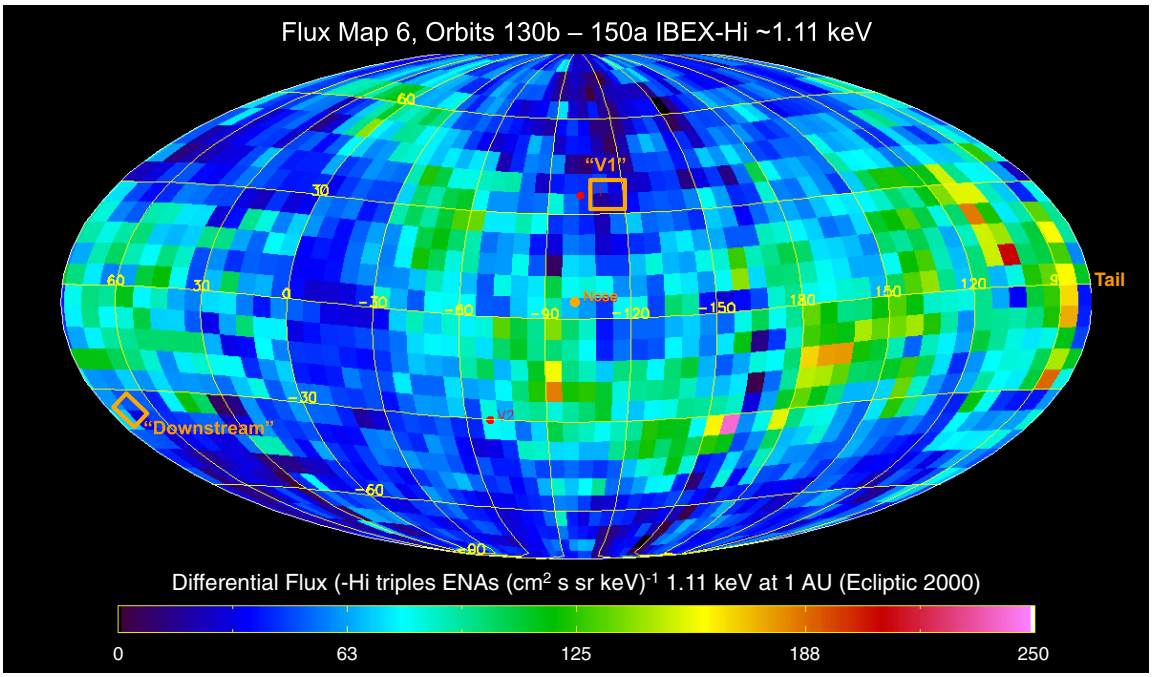

Figure 3. *IBEX-Hi* sky map 6 (Mollweide projection) at 1.11 keV. The center of the map is the direction of the Sun's motion relative to the local interstellar cloud. The *IBEX* Ribbon wraps around this direction from high northern latitude in the upper left to southern latitudes in the middle of the map. Two directions or pixels in the sky (orange rectangles) are selected for study. They are centered approximately in the direction of *Voyager 1*, labeled "V1" and at midlatitudes nearly opposite the nose direction, labeled "Downstream."

(A color version of this figure is available in the online journal.)

region in the sky have Earth's orbital velocity added to (subtracted from) them in February–March (August–September). Furthermore, these observations are susceptible to different near-Earth backgrounds because observations in February are made when the *IBEX* spacecraft is in the solar wind and those in August are made when the spacecraft in Earth's magnetosphere. A very powerful method for distinguishing signal from background is to compare ENA fluxes from two time periods separated by 6 months, after the appropriate frame transformation from the frame moving with the Earth to the inertial frame fixed with the Sun. Fuselier et al. (2012) attempted such a comparison with limited success, especially with *IBEX-Lo* at low energies. The primary difficulty with this attempt was that there were significant backgrounds at low energies associated with ENA measurements when *IBEX* was in Earth's magnetotail.

The purpose of this paper is to revisit this comparison of ENA fluxes at 6 month intervals. When measurement intervals in the magnetosphere are carefully selected, low energy backgrounds in this region are minimized, and ENA fluxes from February and August compare favorably over a wide range of energies. Section 2 describes selection of ENA observations from four intervals, two in August and two in February. It also compares ENA fluxes from the intervals and identifies the range of energies where signal exceeds background. Section 3 transforms the fluxes to 100 AU. It also discusses implications for low energy fluxes measured by *IBEX* and the possibility that the spectrum turns over at low energies. Section 4 presents a summary and conclusions and compares an ion spectrum derived from the ENA fluxes in the *Voyager 1* direction with in situ ion measurements from *Voyager 1*. Appendix A describes how data intervals are selected when *IBEX* was in Earth's magnetotail. Appendix B describes the mathematical tests applied to the energy spectrum to determine if there is evidence of one or more ENA populations.

2. OBSERVATIONS

Figure 3 shows *IBEX-Hi* sky map 6 (combining data from orbits 130b to 150a, from 2011 June 21 to December 29) at 1.11 keV. The sky map is a Mollweide projection nearly in ecliptic coordinates (the center of the projection is the new nose direction, which is at approximately 259° (–95°) ecliptic longitude and approximately +5° ecliptic latitude (Möbius et al. 2012; McComas et al. 2012a)). Fluxes are in the spacecraft frame at the center passband of *IBEX-Hi* energy channel 3 (1.11 keV). Most of the measurements for this sky map were made as the spacecraft orbit precessed through Earth's magnetotail. All data were culled and corrected for several backgrounds, including the variable cosmic ray intensity (McComas et al. 2012b). No reference frame corrections have been applied to this sky map, and the fluxes are shown at 1AU (i.e., without correction for survival against reionization as the neutral atoms propagate from ~100 to 1 AU).

Appendix A provides a detailed discussion of data selection when the spacecraft is in Earth's magnetotail. Data intervals must be selected carefully to avoid regions with high magnetospheric backgrounds and must be selected for specific solar wind conditions that provide favorable magnetotail geometry and plasma conditions. Furthermore, only specific viewing directions of the heliosphere are available for these conditions. Appendix A identifies two viewing directions or pixels in the sky that meet these stringent criteria. These pixels are shown by the orange rectangles in Figure 3, and they are larger than the 6° × 6° pixels in the sky map. The centers of these pixels are near to the direction to the *Voyager 1* spacecraft (labeled "V1" at ecliptic latitude +36°, ecliptic longitude, −115°) and the direction near the downstream (at a longitude opposite the nose) at southern midlatitudes (labeled "downstream" at latitude −42°, longitude +71°).

As discussed in Appendix A, the downstream midlatitude, or simply downstream pixel, was observed in map 2 during parts of orbit 44. These observations were made in August 2009, when the *IBEX* spacecraft was in Earth's magnetospheric lobes. Hereafter, these downstream ENA fluxes are labeled by the location of the spacecraft within the near-Earth environment at the time of the measurements, in this case the "lobe." The corresponding observations 6 months later come from map 3, from parts of orbit 68. These observations were made in 2010 March, when *IBEX* was in the solar wind upstream of Earth's bow shock. Hereafter, these downstream ENA fluxes are labeled also by the location of the spacecraft within the near-Earth environment, in this case the "solar wind."

Also discussed in Appendix A, the V1 pixel was observed in map 6 during parts of orbits 136b and 137b. These observations were made in 2011 August, when the *IBEX* spacecraft was in Earth's magnetospheric lobes. Following the convention described above, fluxes from the V1 pixel from this time period are labeled "lobe." For the V1 pixel, the corresponding observations 6 months later or earlier (i.e., in maps 5 or 7, when *IBEX* was in the solar wind) from the V1 pixel were not available for *IBEX-Lo*. Therefore, observations from map 3, orbit 66 were used. These observations were made in 2010 February, when the *IBEX* spacecraft was in the solar wind. Using observations 18 months apart instead of 6 months apart does not introduce problems in the comparison done here. Although the overall ENA flux decreased over the first three years of *IBEX* operations, the largest decrease in the V1 direction (for energies near 1 keV) was only of the order of 15% over 2 yr from 2009 to 2011 and less than that from 2010 to 2011 (McComas et al. 2012b). These changes in flux are within the statistical uncertainties of the flux comparisons that are done here.

Following the procedure outlined in Fuselier et al. (2012), two corrections are applied successively to the observations. First, *IBEX-Lo* observations are corrected for "sputtering." Second, *IBEX-Lo* and -*Hi* observations are transformed from Earth's frame of reference to the inertial (solar) frame.

For the first correction, the term "sputtering" is used here to include the flux that appears in all lower energy channels from knockoff of ions from the neutral-to-ion conversion surface by higher energy neutrals. Sputtering corrections for *IBEX-Lo* are made starting at the highest energy channel (using the *IBEX-Hi* fluxes as a starting point because they do not contain a sputtering component). ENAs in the highest energy channel of *IBEX-Lo* contribute sputtered flux to all lower energy channels and, in principle, the percentage of sputtered flux should increase with decreasing energy. However, as described in Fuselier et al. (2012), the characteristics of the ENA spectrum and the sputtering efficiency result in an almost constant ~10–20% overall reduction in flux due to sputtering in each *IBEX-Lo* energy channel.

For the second correction, energy and flux are transformed from Earth's frame of reference to the solar inertial frame (hereafter referred to as the inertial frame) by accounting for the 30 km s^{-1} motion of the Earth around the Sun. Following Fuselier et al. (2012), the velocity vector, $\mathbf{v}_i$, of a neutral in the inertial frame is,

$$\mathbf{v}_i = \mathbf{v} + \mathbf{u}_{SC}, \quad (1)$$

where $\mathbf{v}$ is the velocity of the ENA in the *IBEX* spacecraft frame and $\mathbf{u}_{SC}$ is the velocity of the spacecraft, which is simplified to the velocity of the Earth around the Sun. The corresponding energy in the inertial frame is

$$E_i = mv_i^2/2. \quad (2)$$

The distribution function remains unchanged in the frame transformation, so the differential energy flux in the inertial frame is

$$J_i = E_i J/E. \quad (3)$$

Equation (3) shows that fluxes decrease (increase) from the spacecraft frame to the solar inertial frame for sensor views in the same (opposite) direction of Earth's motion. Furthermore, Equations (1)–(3) show that the magnitude of this change is larger for lower energies.

2.1. Observations from the Lines of Sight to the V1 and Downstream Pixels

Figures 4(A) and (B) show the ENA energy spectrum in the inertial frame from the V1 pixel and the downstream pixel, respectively. In Figure 4(A), solid lines and filled symbols show fluxes measured when *IBEX* was in Earth's magnetospheric lobes in 2011 August, while dashed lines connecting open symbols show fluxes measured when *IBEX* was in the solar wind in 2010 February. Red circles show *IBEX-Hi* fluxes, and black squares show *IBEX-Lo* fluxes. Error bars show the larger of either statistical errors or 50% (30%) absolute flux uncertainties for *IBEX-Lo* at energies greater than (less than) 0.1 keV and 20% absolute flux uncertainties for *IBEX-Hi* at all energies. For *IBEX-Lo*, these absolute uncertainties are estimated from the absolute flux uncertainty of the neutral beam used to calibrate the sensor in the laboratory. The absolute flux uncertainty of the low-energy beam that was used is poorly known, and its dependence on energy is likely more complex than assumed here. Therefore, conservative values are used here, consistent with those used previously (Fuselier et al. 2010, 2012). There is an additional, systematic error associated with the frame transformation because the *IBEX* sensor energy channels are very wide (FWHM, $\Delta E/E \sim 0.7$). Because the error in the approximately Gaussian shaped energy channels is $\Delta E/E/2.354$ (Bevington & Robinson 2003), the resulting uncertainty in the ENA flux is much smaller than the 20%–50% absolute uncertainties. Only five *IBEX-Hi* energy channels are shown because there is background contamination in the lowest energy channel (Wurz et al. 2009; Fuselier et al. 2012). This background appears to depend on the ambient electron spectrum and is present when *IBEX* makes measurements both in the solar wind and in the magnetotail.

It is convenient to split up the spectra in Figures 4(A) and (B) into four energy ranges. From lowest to highest these ranges are: less than about 0.1 keV, about 0.1–0.5 keV, 0.5–2 keV, and greater than 2 keV. In these four energy ranges, different tests are applied to identify the heliospheric signal and to understand the nature of the background. In addition, an important assumption (discussed in Section 2.2) is used to understand the nature of the background in the lowest energy range.

In Figure 4(A), at energies greater than 2 keV, the energy ranges of the two sensors do not overlap. However, *IBEX-Hi* fluxes measured when the spacecraft was in the lobe and in the solar wind agree very well with each other after the frame transformation. Since absolute flux uncertainties are small, the good agreement in the fluxes after the frame transformation indicates that the heliospheric signal is larger than any local background moving with the spacecraft or the Earth.

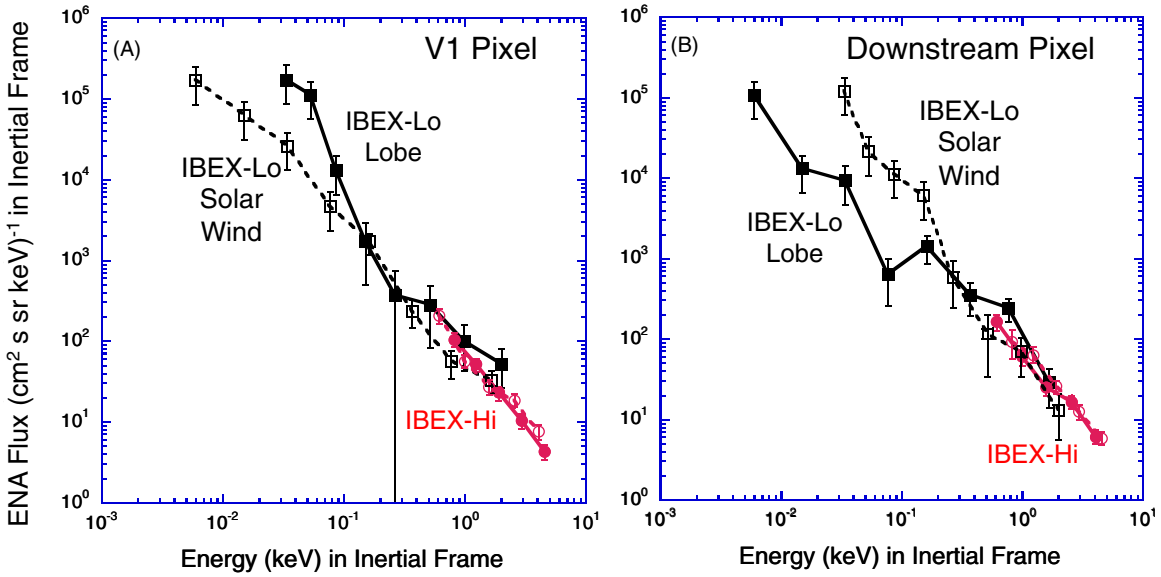

Figure 4. ENA differential energy flux vs. energy in the inertial frame from the V1 pixel (A) and the downstream pixel (B), as indicated in Figure 3. In both pixels, *IBEX-Hi* and -*Lo* fluxes agree well at overlapping energies. At fluxes above about 0.1 keV for the V1 pixel and above 0.13 keV for the downstream pixel, the fluxes measured when *IBEX* was in the solar wind agree well with the fluxes measured when *IBEX* was in the lobe/magnetotail. Below these energies, the fluxes diverge, indicating that there is a background in one or both near-Earth locations that is higher than the heliospheric signal.

(A color version of this figure is available in the online journal.)

At energies between 0.5 and 2 keV, the energy ranges of the two sensors overlap. In this energy range, the *IBEX-Lo* flux and *IBEX-Hi* fluxes are in good agreement with one another (certainly within the uncertainties of the measurements). The fluxes measured when the spacecraft was in the lobe and solar wind also agree reasonably well with one another. Similar fluxes in this inter- and intra-instrument comparison are the strongest evidence that the heliospheric ENA signal is larger than any local background in this energy range. As discussed in the introduction, the sensors are susceptible to different local backgrounds and have different measurement techniques, but they were cross-calibrated in the laboratory. Although a background that results in accidental agreement between two sets of flux measurements from the two different sensors (four independent measurements) is possible, it is not likely.

At energies between about 0.1 and 0.5 keV in Figure 4(A), the energy ranges of the two sensors no longer overlap. However, similar to the comparison of *IBEX-Hi* fluxes at energies greater than 2 keV, *IBEX-Lo* fluxes at energies between about 0.1 and 0.5 keV agree with each another. This agreement is a good indication that the heliospheric fluxes are larger than any local background. Because of the larger uncertainties at these lower energies (compared with the uncertainties at energies greater than 2 keV), the fluxes could still agree if there was a local background that was up to about half of the total flux.

At energies less than 0.1 keV, *IBEX-Lo* fluxes from the lobe and solar wind diverge. This divergence indicates that background is larger than the heliospheric signal in one or both of the near-Earth regions where *IBEX* is making measurements. The nature of this background is revealed in the analysis in Section 2.2.

Figure 4(B) shows the ENA energy spectrum in the inertial frame from the downstream pixel. The format is the same as that for Figure 4(A). The agreement between fluxes in the energy ranges from about 0.1 to 0.5 keV, 0.5 to 2 keV, and greater than 2 keV is also similar to that in Figure 4(A). Thus, the same interpretation applies to the downstream pixel as the V1 pixel. Namely, at energies above about 0.1 keV, the heliospheric signal is larger than the local background. In Figure 4(B), the deviation in the *IBEX-Lo* fluxes measured when the spacecraft was in the lobe and in the solar wind occurs at a higher energy than in Figure 4(A). This difference is interpreted in the next section as an indication of the background level at energies between 0.1 and 0.5 keV.

2.2. *Characteristics of Backgrounds in the IBEX-Lo Measurements at Energies Less than 0.5 keV*

As indicated in Figure 4(A), *IBEX-Lo* fluxes agree at energies between 0.1 and 0.5 keV, but they diverge below 0.1 keV. In Figure 4(B), *IBEX-Lo* fluxes agree at energies between 0.2 and 0.5 keV, but they diverge below 0.2 keV. Fluxes at and below 0.1 keV are measured in the first four energy channels of *IBEX-Lo*, with center energies (in the spacecraft frame) of 0.015, 0.029, 0.055, and 0.11 keV, respectively. The flux divergence in Figures 4(A) and (B) is indicative of a background in one or both near-Earth regions where *IBEX* makes measurements. It is most likely that the source or sources of this background are local: (1) neutrals or negative ions generated by some internal process inside the *IBEX-Lo* sensor, (2) neutrals generated in the near-Earth environment traveling with the Earth or the spacecraft, or (3) neutrals or negative ions generated inside the *IBEX-Lo* sensor by an external ion or neutral source. By comparing fluxes in the spacecraft frame (i.e., the frame moving with the Earth), possible origins of the background are distinguishable. If background is generated internally in the sensor independent of external conditions, then fluxes measured while *IBEX* was in the magnetospheric lobe and in the solar wind upstream of Earth's bow shock should agree. If there is an external, near-Earth origin of the background, then fluxes from the two near-Earth regions should not agree.

Figure 5(A) shows fluxes measured in the spacecraft frame for the first four energy channels for *IBEX-Lo* and the five energy channels for *IBEX-Hi* from the V1 pixel. Figure 5(B) shows these fluxes transformed into the inertial frame. The format for the panels in Figure 5 is the same as that for the panels in Figure 4

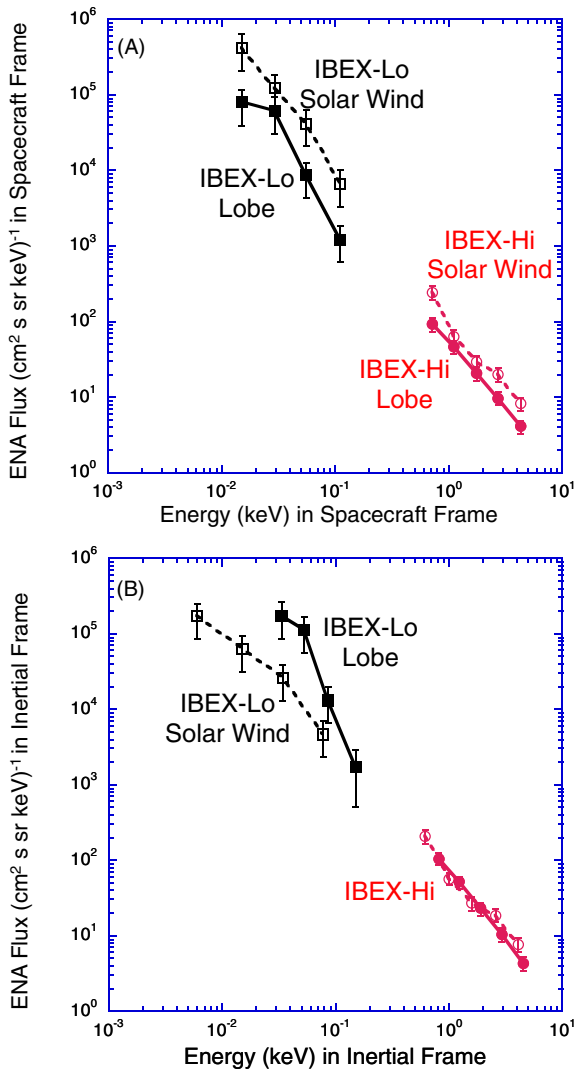

Figure 5. *IBEX-Hi* and *IBEX-Lo* (first four energy channels) ENA fluxes from the V1 pixel in the spacecraft frame (A) and in the inertial frame (B). When *IBEX* was in the solar wind, it measured higher fluxes than when it was in the lobe because the spacecraft was moving in the ENA flow direction when in the solar wind and opposite the ENA flow direction in the lobe. When transformed into the inertial frame, the *IBEX-Hi* fluxes agree, while the *IBEX-Lo* fluxes for the first four energy channels are overcorrected and disagree.

(A color version of this figure is available in the online journal.)

and Figure 5(B) simply reproduces part of the energy spectrum shown in full in Figure 4(A). *IBEX-Lo* fluxes for the four energy channels between 0.2 and 2 keV have been removed for clarity.

As shown in Figure 5(A), fluxes in the spacecraft frame do not agree with one another. Fluxes measured when *IBEX* was in the magnetospheric lobe are consistently lower than those measured when *IBEX* was in the solar wind upstream of Earth's bow shock. Higher fluxes are expected when *IBEX* was in the solar wind because, at the time, the spacecraft was moving toward the ENAs coming from the V1 pixel. Conversely, lower fluxes are expected when *IBEX* was in the magnetospheric lobe because, at the time, the spacecraft was moving away from the ENAs from the V1 pixel. In the transformation from the spacecraft frame to the inertial frame (governed by Equations (1)–(3)), the ENA flux and energy measured when *IBEX* was in the solar wind decrease. Similarly, in this transformation, the ENA flux and energy measured when *IBEX* was in the lobe increase.

For *IBEX-Hi*, the frame-transformed fluxes in Figure 5(B) agree with one another. However, for *IBEX-Lo*, the transformed fluxes do not agree, and there is a switch from Figure 5(A) to Figure 5(B) such that in Figure 5(B), fluxes measured when the spacecraft was the solar wind are now lower than those measured when the spacecraft was in the lobe. This switch indicates that there is a background present that is created by a local source (either neutral or non-neutral) moving with the Earth (or with the spacecraft).

When *IBEX* was in solar wind and viewing the V1 direction, the first four energy channels are known to contain a sputtered signal primarily from interstellar neutral (ISN) helium (Möbius et al. 2009; Saul et al. 2012; Fuselier et al. 2012). ISN helium sputters low energy negative hydrogen ions from the *IBEX-Lo* conversion surface. Since these sputtered negative ions do not retain the energy of the incident (helium) neutral, they are created internally in the sensor, and their fluxes should not be transformed from the spacecraft frame. Again, after frame transformation, Figure 5(B) shows that *IBEX-Lo* fluxes measured when the spacecraft was in the lobe (when no ISN source for sputtered negative ions is present) are higher than fluxes measured when *IBEX* was in the solar wind. Thus, even in the lobe, there is a background source that is moving with the Earth or the spacecraft that is higher than the heliospheric signal at energies below 0.1 keV.

Figure 6(A) shows ENA fluxes measured in the spacecraft frame for the first four energy channels of *IBEX-Lo* and the five energy channels of *IBEX-Hi* from the downstream pixel. Figure 6(B) shows the fluxes in the inertial frame. The format is the same as that for Figure 5.

Similar to Figure 5(A), the ENA fluxes in Figure 6(A) in the spacecraft frame do not agree with one another. However, in Figure 6(A), fluxes measured when *IBEX* was in the magnetospheric lobe are mostly higher than those measured when *IBEX* was in the solar wind upstream of Earth's bow shock. Higher fluxes are expected when *IBEX* was in the lobe in this case because, at the time, the spacecraft was moving toward the ENAs coming from the downstream pixel. Conversely, lower fluxes are expected when *IBEX* was in the solar wind because, at the time, the spacecraft was moving away from the ENAs from the downstream pixel.

For *IBEX-Hi*, the frame-transformed fluxes in Figure 6(B) agree with one another, just as they do in Figure 5(B). However, for the frame-transformed *IBEX-Lo* fluxes in Figure 6(B), the transformed fluxes do not agree. A switch occurs from Figure 6(A) to Figure 6(B) such that in Figure 6(B), fluxes measured when the spacecraft was the solar wind are now higher than those measured when the spacecraft was in the lobe. This switch is similar to the switch from Figure 5 (A) to Figure 5(B) and again indicates that there is a background in *IBEX-Lo* that is created by a local source (either neutral or non-neutral) that is moving with the Earth (or with the spacecraft).

While it is clear that the background level in the first four energy channels of *IBEX-Lo* (up to 0.1 keV) is larger than the heliospheric signal, background levels compared with the heliospheric signal at energies from 0.1 to 0.5 keV are more difficult to determine. To gain some understanding of the background levels at these higher energies, it is assumed here that the background from 0.01 to 0.5 keV is similar in the two view direction in the sky. Support for this assumption comes from comparison of *IBEX-Lo* fluxes in Figures 5(A) and 6(A). Fluxes measured in the spacecraft frame from two different directions in the sky should not necessarily agree. However,

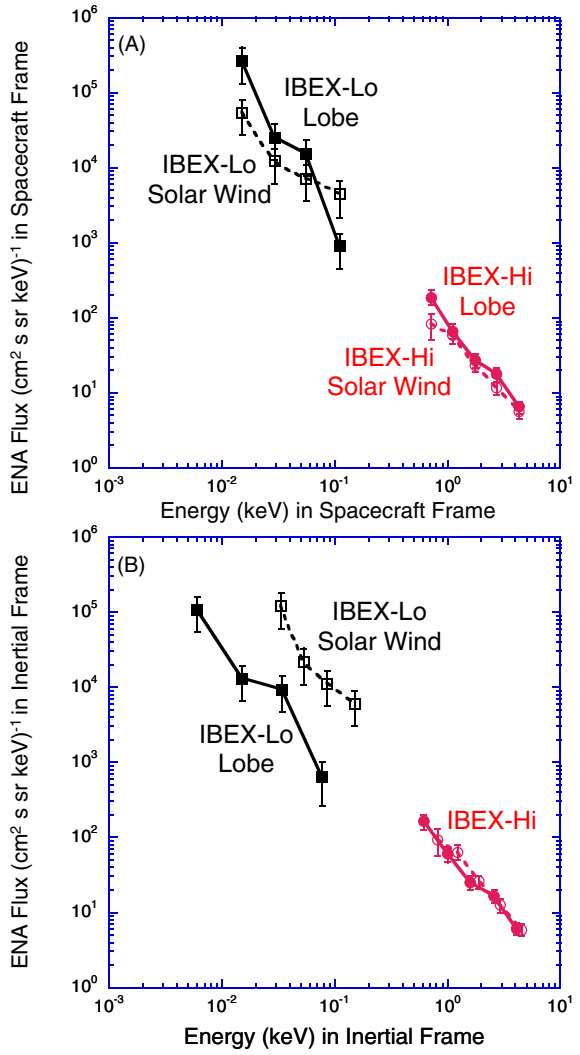

Figure 6. *IBEX-Hi* and *IBEX-Lo* (first four energy channels) fluxes from the downstream pixel in the spacecraft frame (A) and in the inertial frame (B). When *IBEX* was in the lobe, the sensors viewed in the direction of the ENAs from the tail region, and ENA fluxes were generally higher than those measured in the solar wind when *IBEX* was moving in the opposite direction. When transformed into the inertial frame, the *IBEX-Hi* fluxes agree, while the *IBEX-Lo* fluxes for the first four energy channels are overcorrected and disagree.

(A color version of this figure is available in the online journal.)

IBEX-Lo fluxes measured while the spacecraft was in the lobe from the V1 pixel in Figure 5(A) and fluxes from the downstream pixel in Figure 6(A) agree within the uncertainties of the measurements (here the sets of fluxes that were measured when the spacecraft was in the lobe are compared). This agreement suggests that the background (at least in the first four energy channels of *IBEX-Lo*) can be assumed to be independent of view direction, at least for these two directions in the sky.

With this assumption, fluxes in Figures 4(A) and (B) from the V1 and downstream pixels, respectively, can be compared and background levels from 0.1 to 0.5 keV can be estimated. In Figure 4(A), fluxes agree at energies from 0.1 to 0.5 keV, while in Figure 4(B), fluxes agree for energies from 0.2 to 0.5 keV. At 0.15 keV, fluxes in Figure 4(A) are approximately a factor of two to five times higher than at the same energy in Figure 4(B). Therefore, the background could be approximately 50% of the flux at 0.15 keV in Figure 4(A) (i.e., the magnitude of the absolute uncertainties in the measurement). At 0.25 keV, the fluxes agree to within about 30%, so the background could be of the order of 30% of the heliospheric ENA flux at that energy.

The results from the approach adopted here suggest that there is a near-Earth background source that is higher than the heliospheric ENA flux below 0.1 keV in the V1 direction and 0.2 keV in the downstream direction. As a consequence, only upper limits of the flux can be specified for these energies. Upper limits are taken to be the lowest fluxes measured in the spacecraft frame. No frame transformation is made to these upper limits because fluxes are dominated by local backgrounds that should not be transformed into the inertial frame.

3. ENA FLUXES AT 100 AU AND IMPLICATIONS FOR INNER HELIOSHEATH PLASMA PARAMETERS

Figures 4(A) and (B) show ENA fluxes in the inertial frame measured at 1 AU. To transform these fluxes to 100 AU (the nominal distance to the source region), survival of neutrals against reionization from 100 AU to 1 AU must be accounted for. Hydrogen ENAs traveling from 100 AU to 1 AU are subject to ionization losses. Losses propagating from about 150 to 100 AU are minimal, but losses propagating from 100 AU are significant, especially within the last ∼5 AU of the Sun. ENA survival is energy, solar cycle, and latitude dependent (Bzowski 2008). Following McComas et al. (2012b), survival estimates and uncertainties were calculated for all energies using the ionization and radiation pressure factors from Sokół et al. (2013) and Bzowski et al. (2013b). Table 1 shows the best flux values at 1 AU from Figure 4(A), the survival (% of neutrals that survive to 1 AU), and fluxes and uncertainties at 100 AU for the V1 pixel. Uncertainties in the flux at 100 AU are a combination of flux uncertainties at 1 AU and uncertainties in the survival. For a given survival probability, the uncertainty is actually asymmetric with larger negative uncertainty than positive uncertainty (Bzowski et al. 2013a). In addition, the flux at about 0.1 keV has a larger negative uncertainty on the basis of the assessment of the background between 0.1 and 0.2 keV in the previous section. Table 2 shows the same data but from the downstream pixel.

Figures 7(A) and (B) show the ENA flux spectrum (final three columns of Tables 1 and 2) over the full energy range from the V1 and downstream pixels, respectively. Bars with downward directed arrows show upper limits on these fluxes at the lowest energies.

Comparing the two directions in the sky, the fluxes at energies greater than 0.2 keV are very similar. In fact, the same function can be fit to both spectra. Between 0.1 and 0.2 keV, fluxes in the V1 pixel are about a factor of two to five greater than the upper limit flux in the downstream region. The lower fluxes in the downstream pixel between 0.1 and 0.2 keV are consistent with an ENA flux distribution that is more than an order of magnitude lower than the one in the V1 pixel.

In Figure 7(A) there is a suggestion of a break in the energy spectrum at about 0.4 keV. This possible break occurs at an energy that is just below the lower energy range of *IBEX-Hi*. Appendix B contains a test that determines whether two power laws or one power law is more likely to fit the ENA energy spectrum. The result is that this apparent break in the spectrum cannot be used to differentiate two (or more) power laws for the ENA spectrum over the entire energy range from 0.1 to 6 keV. To be sure, there are different ENA populations from different parent ion populations over this energy range. Figure 1 shows that several populations are created by different charge exchange processes. However, the energy overlap of these populations is

Table 1
Energies and Fluxes from the V1 Pixel at 1 AU and 100 AU

Sensor/Energy Channel	Energy (keV) in Inertial Frame	Flux at 1 AU (cm^2 s sr keV)$^{-1}$ in Inertial Frame	Uncertainty in Flux at 1 AU	Survival Probability (%)	Uncertainty in Survival Probability	Flux at 100 AU (cm^2 s sr keV)$^{-1}$ in Inertial Frame	Uncertainty in Flux at 100 AU
1-Lo	0.015	2.6E+05[a]	1.31E+05	0.265	0.035	9.8E+05[a]	5.11E+05
2-Lo	0.029	25500[a]	12700	0.343	0.036	7.4E+04[a]	3.79E+04
3-Lo	0.055	15400[a]	7710	0.427	0.035	3.6E+04[a]	1.83E+04
4-Lo	0.078	4690	2340	0.454	0.033	1.03E+04	5.21E+03
5-Lo	0.163	1690	508	0.568	0.029	2.98E+03	9.08E+02
5-Lo	0.264	374	374	0.597	0.028	6.26E+02	6.27E+02
6-Lo	0.370	236	89.1	0.678	0.025	3.48E+02	1.32E+02
2-Hi	0.808	106	21.2	0.729	0.021	1.45E+02	2.94E+01
3-Hi	1.232	51.6	10.3	0.768	0.019	6.72E+01	1.35E+01
4-Hi	1.891	22.9	4.57	0.802	0.016	2.86E+01	5.73E+00
5-Hi	2.918	10.4	2.09	0.832	0.014	1.25E+01	2.52E+00
6-Hi	4.525	4.32	0.865	0.858	0.012	5.03E+00	1.01E+00

Note. [a] Flux upper limit

Table 2
Energies and Fluxes from the Downstream Pixel at 1 AU and 100 AU

Sensor/Energy Channel	Energy (keV) in Inertial Frame	Flux at 1 AU (cm^2 s sr keV)$^{-1}$ in Inertial Frame	Uncertainty in Flux at 1 AU	Survival Probability (%)	Uncertainty in Survival Probability	Flux at 100 AU (cm^2 s sr keV)$^{-1}$ in Inertial Frame	Uncertainty in Flux at 100 AU
1-Lo	0.015	54000[a]	27000	0.091	0.019	5.9E+05[a]	3.23E+05
2-Lo	0.029	12000[a]	6000	0.215	0.030	5.5E+04[a]	2.91E+04
3-Lo	0.055	7220[a]	3560	0.353	0.033	2.1E+04[a]	1.03E+04
4-Lo	0.11	885[a]	442	0.481	0.033	1.8E+03[a]	9.28E+02
5-Lo	0.264	580	335	0.648	0.025	8.95E+02	5.18E+02
5-Lo	0.37	353	158	0.593	0.029	5.95E+02	2.68E+02
2-Hi	0.621	164	36.5	0.747	0.020	2.20E+02	4.92E+01
3-Hi	0.998	60.1	13.3	0.787	0.018	7.64E+01	1.70E+01
4-Hi	1.598	25.3	5.05	0.821	0.015	3.08E+01	6.18E+00
5-Hi	2.551	16.8	3.37	0.852	0.013	1.97E+01	3.97E+00
6-Hi	4.065	6.16	1.23	0.875	0.011	7.04E+00	1.41E+00

Note. [a] Flux upper limit

sufficient to produce an apparent continuous ENA spectrum described by a single power law.

Livadiotis et al. (2011) used the fact that the spectrum from ~0.7 to 6 keV can be characterized by a kappa distribution to derive temperatures and densities for the parent ion distribution in the inner heliosheath. The temperatures were quite low (2.2×10^5 K in the V1 direction in the sky), indicating that the kappa distribution is effectively extended to energies well below 0.7 keV. This work extends the ENA energy spectrum down to ~0.1 keV, and as Appendix B shows, the spectrum can still described by a single function. Below ~0.1 keV, only upper limits on the energy spectrum are known. Also shown in Figures 7(A) and (B) are upper limits for the ENA flux that were obtained from Lyman-alpha absorption observation from stars approximately in the "upwind" direction and in the center of the heliotail direction (Wood & Izmodenov 2010; Wood et al. 2007). The form of the upper limits to the ENA fluxes are not known from the Lyman-alpha observations and Figure 7 shows two different limits that are consistent with these absorption measurements. Also, there are no stars in the V1 direction or directly in the downstream direction to determine the Lyman-alpha absorption. Therefore, the upper limits in Figures 7(A) and (B) come from two stars that are in the "cross-wind" direction 123° from the nose direction in Figure 2 for the V1 direction and stars in the direction opposite the nose but nearly in the ecliptic plane for the downstream direction. Since the heliosheath may be thicker in the cross-wind direction than in the V1 direction in particular, the absorption is likely greater. Therefore, estimates in Figure 7 represent conservative upper limits, especially for the V1 direction.

These upper limits, combined with the ENA upper limits from *IBEX*, place important constraints on the shape of the ENA spectrum below 0.1 keV. For the V1 pixel, the upwind Lyman-alpha limit and the background upper limits at 0.057 keV and 0.027 keV indicate that the ENA flux must deviate from the single kappa distribution below 0.1 keV. In particular, the ENA flux at 0.057 keV must not be a significant fraction of the measured background flux. Dashed lines in Figure 7(A) illustrate the resulting turnover of the energy spectrum at low energies. The dashed line labeled "50% background" in Figure 7(A) shows spectral turnovers that are consistent with up to 50% background in the fluxes at 0.1 keV.

For the ENA spectrum from the downstream pixel, the constraints are more severe. The ENA flux at 0.11 keV must be substantially below the background upper limit at that energy. Thus, the spectrum must have a relatively sharp turnover below 0.2 keV, as illustrated in Figure 7(B) by the dashed lines. Similar to Figure 7(A), the turnover labeled "50% background" shows the spectrum consistent with up to 50% background in the fluxes at 0.2 keV.

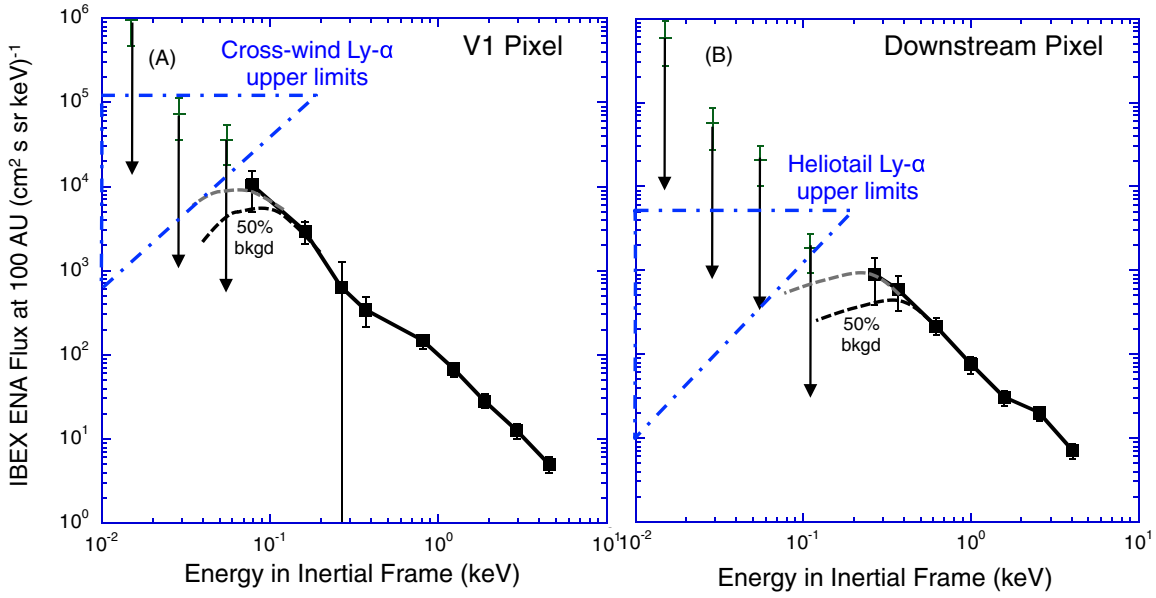

Figure 7. Combined *IBEX-Hi* and *-Lo* ENA fluxes from the V1 pixel (A) and the downstream pixel (B) corrected for survival probability and transformed to 100 AU. Fluxes at energies less than 0.1 keV are shown with downward arrows because they are only upper limits based on the background fluxes in Figure 4. There is a possible break in the V1 pixel energy spectrum at approximately 0.3 keV. However, fluxes generally increase almost linearly (on the log-log scale) across the energy spectrum, and fluxes at energies greater than 0.2 keV are very similar from both directions in the sky. Two possible spectral profiles below 0.2 keV from the downstream pixel (dashed lines) are consistent with the upper limits of the fluxes less than 0.2 keV and a small background or a background that is 50% of the total flux at about 0.2 keV. Similar possible spectral profiles (dashed lines) occur at and below about 0.1 keV in the spectrum from the V1 pixel. Thus, the two spectra likely differ at energies below 0.2 keV.

(A color version of this figure is available in the online journal.)

The turnover of the ENA spectrum at energies below 0.1 keV in the V1 direction is consistent with the single kappa distribution fit to the spectrum up to 6 keV (Livadiotis et al. 2013). The turnover energy for all sky directions was calculated (see Figure 5 of Livadiotis et al. 2013), and the values of this turnover were all less than ∼0.1 keV.

4. SUMMARY AND CONCLUSIONS

Using observations from two different vantage points in Earth's orbit, the heliospheric signal is separated from near-Earth backgrounds in the *IBEX* energy range. For the V1 pixel, the heliospheric signal dominates the *IBEX* observations at energies above about 0.1 keV. For the downstream pixel, the heliospheric signal is higher than background above about 0.2 keV. Below these energies, a near-Earth background is higher. By assuming that the background is similar for the two view directions in the sky, the background between 0.1 keV and 0.2 keV is estimated to be of the order of 50% of the total signal in the V1 pixel, and the background is larger than the signal in the downstream direction. This background level depends on the absolute uncertainties in the flux measurements and these uncertainties are not well known for *IBEX-Lo*.

Although a near-Earth background is higher at energies below 0.1 keV, the upper limits on the ENA fluxes (obtained from the background estimates as well as from Lyman-Alpha measurements (Wood & Izmodenov 2010; Wood et al. 2007)) indicate that the ENA spectrum in the two directions in the sky turns over. The turnover occurs at a higher energy in the downstream pixel than in the V1 pixel (Figure 7), indicating that fluxes at energies below about 0.2 keV are lower in the downstream direction than in the V1 direction. These observations have important implications on the nature of the parent ion populations in the inner heliosheath. In particular, it is difficult to explain the ENA fluxes at energies from about 0.1 to 0.2 keV in the V1 pixel without invoking a significant reduction in the radial velocity of the ion distribution, significant turbulence in the inner heliosheath, an additional ENA source outside of the inner heliosheath, and/or some other process. However, with the turnover in the energy spectra in Figure 7, this explanation has become easier.

These results establish the ENA energy spectrum in two directions in the sky from about 0.1 to 6 keV. Over this energy range, the ENA spectrum in these two directions is well described by a single function (e.g., a power law or kappa function). Livadiotis et al. (2013) investigated a single kappa function fit for energies from 0.7 to 6 keV, and the results here, extending down to 0.1 keV, are still consistent with their results. This energy range from 0.1 to 6 keV covers the energies of all the predicted parent ion populations in the inner heliosheath (see Figure 1). There is considerable energy overlap in these populations, but they include (in order of increasing energy) the shocked solar wind, pickup ions created in the inner heliosheath, pickup ions created in the solar wind and convected across the termination shock, and termination shock/heliosheath turbulence accelerated ions. A fifth parent population, namely pickup ions created in the outer heliosheath, may be an additional source for the low energy neutrals between 0.1 and 0.3 keV/e (Desai et al. 2014; Heerikhuisen et al. 2013). The ion spectrum at energies greater than 6 keV is also remarkably smooth. Figure 8 shows an ion energy spectrum in the *Voyager 1* direction that is a combination of *IBEX* (this work), *Cassini* (Krimigis et al. 2009), and *Voyager 1* measurements (Stone et al. 2013; Krimigis et al. 2013). For this spectrum, ENA fluxes from *IBEX* and *Cassini* were converted to ion fluxes using the charge exchange cross sections from Lindsay & Stebbings (2005) and by a simple assumption of a constant ion density in the inner heliosheath and a line of sight integration of 50 AU.

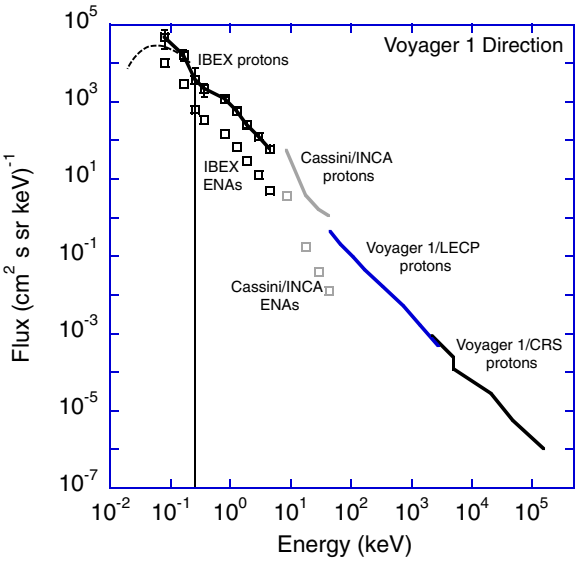

Figure 8. Composite ion and ENA spectrum from the *Voyager 1* direction in the sky. The ENA fluxes from *IBEX* and *Cassini* were converted to ion fluxes assuming a constant ion density in the inner heliosheath and a line of sight integration of 50 AU. The spectrum is remarkably smooth over more than 6 decades in energy and almost 11 decades in flux. The turnover in the spectrum occurs only at the lowest energies and probably starts at or slightly greater than 0.1 keV.

(A color version of this figure is available in the online journal.)

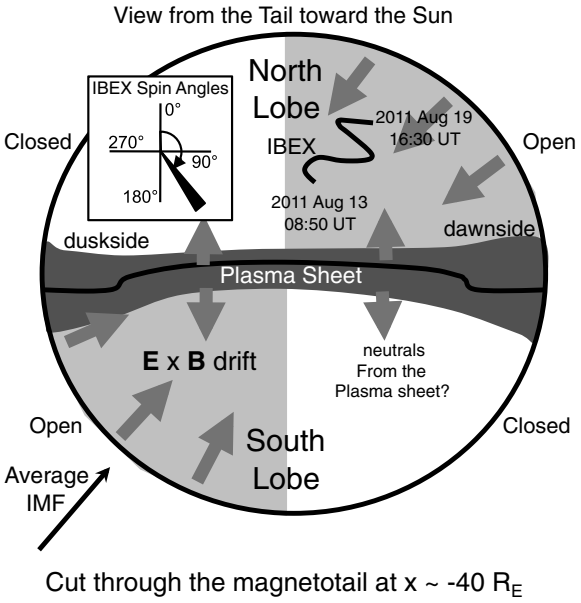

Figure 9. Schematic cross section of Earth's magnetotail about 40 R_E from the Earth. The view is toward the Sun. Low energy ions enter the magnetosphere on the dayside and on the flanks of the magnetopause through open field lines. For the average IMF shown, these ions can drift into the lobe in the two quadrants shown. The other two quadrants are devoid of these low energy ions. Possible sources of background in heliospheric ENA measurements include these low energy ions and neutrals created by charge exchange of low energy ions from the lobes or plasma sheet. Careful selection of intervals with stable IMF and careful selection of view directions minimizes these backgrounds.

Over 7 orders of magnitude in energy and 11 orders of magnitude in flux, the spectrum is described by a power law. It is only at energies less than about 0.1 keV that the ion spectrum probably turns over.

Support for this study comes from NASA's Explorer program. *IBEX* is the result of efforts from a large number of scientists, engineers, and others. All who contributed to this mission share in its success. Solar wind data used to determine the IMF conditions, and the choice of lobe intervals in this study are from the *ACE* spacecraft solar wind monitors (PIs: D. McComas and E. Smith) via the CDAWeb. The authors from SRC PAS were supported by grant 2012-06-M-ST9-00455 from the Polish National Science Center.

APPENDIX A

The lobes of Earth's geomagnetic tail are bounded by Earth's magnetopause and located above and below the plasma sheet. From the standpoint of ENA observations above 1 keV, the lobes are an ideal observing location. They are regions of low plasma beta, which implies low plasma densities and high magnetic fields. Because the magnetic field lines that thread the lobes are either "open" or have been open in the past, they are devoid of energetic plasma ions and electrons. Thus, they are free of any local energetic particle foreground in ENA images. Without this foreground, ENA fluxes from a distant source can be detected. Indeed, the first measurements of ENAs from the near-Earth region were made by an energetic particle instrument on International Sun–Earth Explorer spacecraft that was in the lobes (Roelof 1987).

Magnetic reconnection at Earth's dayside magnetopause has a dominant effect on the structure of the lobes and the properties of the plasma within them. Gosling et al. (1985) noted that plasma densities in the northern and southern lobes differed by a factor of 10 or more. Furthermore, density differences were observed in different quadrants of the lobes, and these differences were correlated with the orientation of the interplanetary magnetic field (IMF). Gosling et al. (1985) were able to associate density differences in the lobe with magnetic reconnection at the dayside magnetopause, convection of reconnected field lines into the tail lobes, and **E**×**B** drift of plasma through the open magnetopause and into the lobes.

Figure 9 is a schematic representation of the lobe density structure that results from dayside magnetic reconnection. This cross section of the magnetotail at ∼40 Earth Radii (R_E) from the Earth splits the lobes into four quadrants. For the average IMF orientation shown in Figure 9, the upper right quadrant of the north lobe and the lower left quadrant of the south lobe are associated with open magnetic field lines. The other two lobes are associated with closed magnetic field lines. In the open quadrants, low energy plasma from Earth's dayside and low energy plasma from the high latitude magnetopause on the nightside can **E**×**B** drift into the lobes. This plasma has energies of about 0.3 keV (Hirahara et al. 1997) and, while convecting tailward, can also have a significant drift toward the plasma sheet.

The presence of this plasma in an otherwise low density, very low energetic particle flux region is a significant complication for heliospheric ENA observations at low energies in the lobes. The difficulties are particularly acute for *IBEX-Lo*, which does not reject ions above about 0.2 keV from entering the sensor. *IBEX-Lo* was supposed to have a positive high voltage on its collimator. However, this voltage failed during commissioning. The sensor has an internal deflection voltage for low energy ions (less than about 0.2 keV), but higher energy ions can enter the sensor and sputter low energy negative hydrogen off the

conversion surface, creating a background. Above ~15 keV, ion fluxes are detected in the *IBEX* background monitor (Funsten et al. 2009a; Allegrini et al. 2009). Therefore, for intervals when *IBEX* is in the plasma sheet (which contains hot, dense plasma with energies up to tens of keV), the background monitor flux is used to eliminate these intervals. However, any ions between 0.2 and 15 keV, like those encountered in Earth's lobes, create a potential background in *IBEX-Lo* and are not detected in the *IBEX* background monitor.

Even if these low energy ions could be rejected, there is also a small flux of neutrals at energies below 0.3 keV that result from charge exchange of low energy ions in the lobe with Earth's geocorona. These neutrals are indistinguishable from neutrals from the heliosphere at the same energies. To reduce background from low energy ions and neutrals in the lobe, data interval and view angles must be carefully chosen. For example, in Figure 9, the apparent *IBEX* trajectory in the cross section of the magnetotail from 2011 August 13–19 is shown. During this time in orbit 136b, there are long intervals when the IMF orientation (convected from the *ACE* spacecraft solar wind monitor to the location of *IBEX* in the magnetotail) was within about 40 degrees of the orientation shown in Figure 9. For that magnetic field orientation, the open lobe quadrants (which are regions with ion distributions $\mathbf{E}\times\mathbf{B}$ drifting into the lobe) should be in the upper right and lower left. The small inset in the magnetotail cross section shows the *IBEX* sensor spin angles. *IBEX* views 360°, essentially normal to the magnetotail axis. For the orientation of the IMF shown, one would expect higher background levels for spin angles from 0° to 90° and from 180° to 270°. Furthermore, if there are neutrals from charge exchange of plasma sheet ions, they may also appear in spin angles from 90° to 180°. Thus, for this particular IMF orientation and *IBEX* spacecraft location, only the quadrant from 270° to 360° is available for viewing heliospheric neutrals at low energies. Similar conditions occurred during orbit 137b. These two orbits combined provided the intervals for observing the near- *Voyager 1* direction in Figure 2.

During orbit 44, from 2009 September 6–9, *IBEX* was in the southern lobe in the lower left hand quadrant of Figure 9. There were long intervals (hours at a time over several days) when the IMF average orientation was the same as shown in Figure 9. For these intervals, the available spin angles for viewing heliospheric neutrals were between 90° to 180°. This orbit provided the intervals for observing the downstream direction in Figure 2.

APPENDIX B

STATISTICAL TESTS OF ONE VERSUS TWO ENA POWER LAW SPECTRUM IN THE V1 DIRECTION

In this appendix, the *IBEX-Hi* and *-Lo* fluxes in the V1 direction in the sky (Figure 7(A)) are examined to determine if they are characterized by one or two statistical populations described by different polynomial laws. To do this examination, statistical tests are applied on the following two null-hypotheses:

$H_0(1)$. Both *IBEX-Hi* and *IBEX-Lo* spectra are described by a single polynomial law.
$H_0(2)$. IBEX-Hi and *IBEX-Lo* spectra are described by two different polynomial laws.

Each of the null-hypotheses is tested using a statistical method to rate the goodness of the involved fit. In particular, a good fit of a single polynomial law favors $H_0(1)$, while a good fit of two different polynomial laws, different for *IBEX-Hi* and *IBEX-Lo*, favors $H_0(2)$. Here, two statistical methods used to rate the goodness of a fitting are the "reduced chi-square" and the "*p*-value of the extremes" (e.g., Livadiotis 2014). Both methods are applicable when the errors are normally distributed.

For the chi-square method, the goodness of a fit is estimated by the reduced chi-square value, $\chi^2_{\rm red} = (1/M)\chi^2_{\rm est}$, where M are the degrees of freedom. The meaning of $\chi^2_{\rm red}$ is the portion of χ^2 that corresponds to each of the degrees of freedom, and this has to be ~1 for a good fit. Therefore, a fit is characterized as "good' when $\chi^2_{\rm red} \sim 1$, otherwise there is an overestimation ($\chi^2_{\rm red} < 1$) or underestimation, ($\chi^2_{\rm red} > 1$) of the errors.

For the *p*-value method, the goodness of the fit is evaluated by comparing the estimated chi-square value, $P(\chi^2_{\rm est} \leqslant \chi^2 < \infty)\,\chi^2_{\rm est}$, and the chi-square distribution, $P(\chi^2; M) = (2^{-(M/2)}/\Gamma(M/2))\,e^{-(1/2)\chi^2}(\chi^2)^{(M/2)-1}$, that is the distribution of all the possible χ^2 values (parameterized by the degrees of freedom M). The likelihood of having a χ^2 value, equal to or larger than the estimated value $\chi^2_{\rm est}$, is given by the complementary cumulative distribution. The probability of taking a result χ^2, larger than the estimated value $\chi^2_{\rm est}$, defines the *p*-value that equals $P(\chi^2_{\rm est} \leqslant \chi^2 < \infty) = \int_{\chi^2_{\rm est}}^{\infty} P(\chi^2; M)\,d\chi^2$. The larger the *p*-value, the better the fit. A *p*-value larger than 0.5 corresponds to $\chi^2_{\rm est} < M$ or $\chi^2_{\rm red} < 1$. Larger *p*-values, up to $p = 1$, correspond to smaller chi-squares, down to $\chi^2_{\rm red} \sim 0$. Thus, an increasing *p*-value above the threshold of 0.5 cannot lead to a better fitting. Rather, it leads to a worse fit, similar to a decreasing $\chi^2_{\rm red} < 1$. For this reason, the "*p*-value of the extremes" is used. According to this method, the probability of taking a result, χ^2, that is more extreme than the observed value, $\chi^2_{\rm est}$, defines the *p*-value that equals the minimum between the two probabilities, $P(0 \leqslant \chi^2 \leqslant \chi^2_{\rm est})$, and its complementary, $P(\chi^2_{\rm est} \leqslant \chi^2 < \infty)$. A null hypothesis associated with a *p*-value smaller than the significance level of ~0.05 is typically rejected.

For the fluxes in Figure 6(A), the fitting of $\log J_i \pm \sigma_i$ to the model $V(\log\varepsilon_i; \{\alpha_k\}_{k=1}^{S}) = \sum_{k=0}^{S}\alpha_k\,(\log\varepsilon_i)^k = \alpha_0 + \alpha_1\log\varepsilon_i + \alpha_2(\log\varepsilon_i)^2 + \ldots + \alpha_S(\log\varepsilon_i)^S$, for $i = 1, 2, \ldots, N$, involves minimizing the chi-square $\chi^2(\{\alpha_k\}_{k=0}^{S}) = \sum_{i=1}^{N}\sigma_i^{-2}[\log J_i - \sum_{k=0}^{S}\alpha_k\,x_i^k]^2$. The variance of the flux logarithm $\log J_i$ is given by $\sigma_i^2 = (\delta\log J_i)^2 = (\log e)^2(\delta J_i/J_i)^2$, and the presented methodology is based on the fact that the flux logarithm follows a quasi-normal distribution (i.e., the flux itself follows log-normal statistics (see Livadiotis 2014). For most of the ENA fluxes in the sky, the *IBEX* spectra are well fitted by a linear law on a log-log scale (Livadiotis et al. 2011), while the values of the curvature are relatively small (Livadiotis et al. 2012). Thus, for the fluxes in Figure 6(A), the presented statistical tests are restricted to the linear $V(\log\varepsilon_i; \alpha_0, \alpha_1) = \alpha_0 + \alpha_1\log\varepsilon_i$ and parabolic models $V(\log\varepsilon_i; \alpha_0, \alpha_1, \alpha_2) = \alpha_0 + \alpha_1\log\varepsilon_i + \alpha_2(\log\varepsilon_i)^2$. While the test for a single polynomial is trivial, some extra care is needed for the two-polynomial test: The fit for the *IBEX-Lo* spectrum uses four (4) data points from energy steps 4-Lo (1), 5-Lo (2), and 6-Lo (1) in Table 1. The fluxes from the first three rows in Table 1 are not used because they represent upper limits on the heliospheric flux and are probably dominated by a near-Earth background. The fit for the *IBEX-Hi* spectrum uses five data points, from energy steps 2-Hi to 6-Hi in Table 1, and it has to get connected to the *IBEX-Lo* spectrum, so it includes the last *IBEX-Lo* data point (energy step 6-Lo). Thus, the *IBEX-Hi* spectrum uses six data points. In total, the two-population fitting uses 10 data points, and the model has five parameters

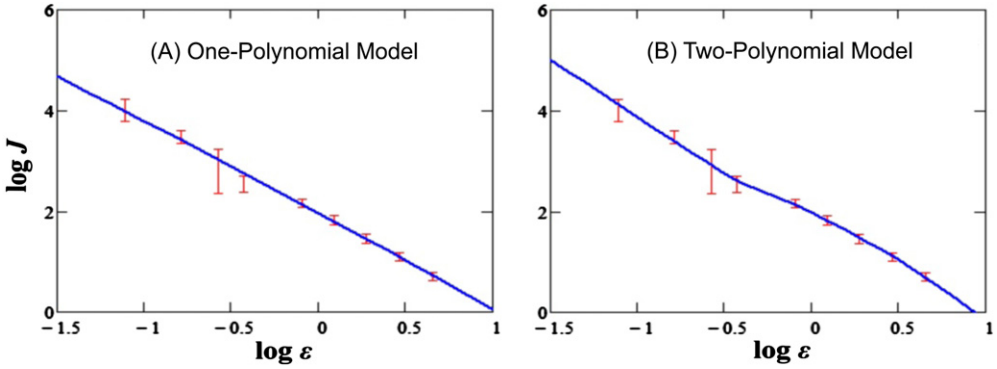

Figure 10. Fitting of one and two power laws to spectra in the V1 pixel.
(A color version of this figure is available in the online journal.)

Table 3
Fitting Characterization of One and Two Polynomials

ONE-Polynomial, $H_0(1)$			TWO-Polynomial, $H_0(2)$		
Model	Reduced Chi-square	p-value	Model	Reduced Chi-square	p-value
Linear	0.397	0.095	Linear–Parabolic	0.120	0.055
Parabolic	0.448	0.153	Parabolic–Parabolic	0.057	0.033

for the linear-parabolic model (linear model for the *IBEX-Lo* and parabolic model for the *IBEX-Hi*) or six parameters for the parabolic-parabolic model.

The results show that both null-hypotheses, $H_0(1)$ and $H_0(2)$, are accepted, i.e., the single polynomial and two-polynomial models are likely. The single polynomial model has somewhat higher chi-square than the two polynomial models. In particular, Table 3 shows that (1) $\chi^2_{\rm red} = 0.448$ and $p = 0.153$ for a single polynomial described by a parabolic model and (2) $\chi^2_{\rm red} = 0.12$ and $p = 0.055$ for two polynomials described by a linear model for the *IBEX-Lo* spectrum and a parabolic model for the *IBEX-Hi* spectrum. Although not shown, these are the highest p-values, and other polynomial combinations lead to smaller p-values. Table 3 summarizes these results, and Figure 10 shows spectra for the one and two population fitting with the highest p-values.

To investigate the statistical sensitivity of the results in Table 3, *IBEX-Lo* uncertainties in Table 1 are multiplied by a scale factor s. The p-values were calculated for both the one- and two-polynomial hypotheses. The results (not shown here) indicate that the conclusions in Table 3 are characterized as "statistically stable" with regards to the comparably large uncertainties associated with *IBEX-Lo* fluxes.

It is important to note that the statistical analysis in this appendix investigates whether the spectrum in Figure 7(A) is composed of different "statistical" polynomials. In reality, the ENA spectrum is not a single ENA population, since it is composed of ENA from a large number of proton sources (possibly five or more overlapping parent populations, as discussed in the introduction). The important point of this mathematical analysis is that it demonstrates that the apparent break in the spectrum in Figure 7(A) is not significant and cannot be used as evidence for multiple ENA populations.

REFERENCES

Allegrini, F., Crew, G. B., Demkee, D., et al. 2009, SSRv, 146, 105
Bevington, P. R., & Robinson, D. K. 2003, Data Reduction and Error Analysis for the Physical Sciences (New York: McGraw-Hill)
Bzowski, M. 2008, A&A, 488, 1057
Bzowski, M., Sokół, J. M., Kubiak, M. A., & Kucharek, H. 2013a, A&A, 557, A50
Bzowski, M., Sokół, J. M., Tokumaru, M., et al. 2013b, in Cross-Calibration of Past and Present Far UV Spectra of Solar System Objects and the Heliosphere, Solar Parameters for Modeling the Interplanetary Background, ed. R. M. Bonnet, E. Quémerais, & M. Snow (ISSI Scientific Report Series 13; New York: Springer), 67
Chalov, S. V., Alexashov, D. B., McComas, D., et al. 2010, ApJL, 716, L99
Chalov, S. V., & Fahr, H. J. 2000, A&A, 360, 381
Chalov, S. V., Fahr, H. J., & Izmodenov, V. V. 2003, JGRA, 108, 1266
Desai, M., Allegrini, F. A., Bzowski, M., et al. 2014, ApJ, 780, 98
Fahr, H.-J., Siewert, M., McComas, D. J., & Schwadron, N. A. 2011, A&A, 531, A77
Funsten, H. O., Allegrini, F., Bochsler, P., et al. 2009a, SSRv, 146, 75
Funsten, H. O., Allegrini, F., Crew, G. B., et al. 2009b, Sci, 326, 964
Fuselier, S. A., Allegrini, F., Bzowski, M., et al. 2012, ApJ, 754, 14
Fuselier, S. A., Allegrini, F., Funsten, H. O., et al. 2009a, Sci, 326, 962
Fuselier, S. A., Bochsler, P., Chornay, D., et al. 2009b, SSRv, 146, 117
Fuselier, S. A., Funsten, H. O., Heirtzler, D., et al. 2010, GeoRL, 37, L13101
Gloeckler, G., & Fisk, L. A. 2010, in AIP Conf. Proc. 1302, Proton Velocity Distributions in the Inner Heliosheath Derived from Energetic Atoms Measured with Cassini and IBEX, ed. J. A. LeRoux et al. (Melville, NY: AIP), 110
Gosling, J. T., Baker, D. N., Bame, D. N., et al. 1985, JGR, 90, 6354
Gruntman, M. A., Roelof, E. C., Mitchell, D. G., et al. 2001, JGR, 106, 15767
Heerikhuisen, J., Pogoreleov, N., Zank, G. P., et al. 2010, ApJL, 708, L126
Heerikhuisen, J., Zernstein, E. J., Kawamura, A. D., Pogoreleov, N., & Zank, G. P. 2013, in AIP Conf. Proc. 1539, Solar Winds 13, ed. G. P. Zank et al. (Melville, NY: AIP), 319
Hirahara, M., Terasawa, T., Mukai, T., et al. 1997, JGR, 102, 2359
Izmodenov, V. V., Alexashov, D. B., Chalov, S. V., et al. 2009, SSRv, 146, 329
Krimigis, S. M., Decker, R. B., Roelof, E. C., et al. 2013, Sci, 341, 144
Krimigis, S. M., Mitchell, D. G., Roelof, E. C., Hsieh, K. C., & McComas, D. J. 2009, Sci, 326, 971
Kucharek, H., Fuselier, S. A., Wurz, P., et al. 2013, ApJ, 776, 109
Lindsay, B. G., & Stebbings, R. F. 2005, JGRA, 110, A12213
Livadiotis, G. 2014, J. Stat. Dist. & Appl., in press
Livadiotis, G., McComas, D. J., Dayeh, M. A., Funsten, H. O., & Schwadron, N. A. 2011, ApJ, 734, 1
Livadiotis, G., McComas, D. J., Randol, B., et al. 2012, ApJ, 751, 64
Livadiotis, G., McComas, D. J., Schwadron, N. A., Funsten, H. O., & Fuselier, S. A. 2013, ApJ, 762, 134
Malama, Y. G., Izmodenov, V. V., & Chalov, S. V. 2006, A&A, 445, 693
McComas, D. J. 2012, in AIP Conf. Proc. 1500, Update on IBEX and the Outer Boundary of the Space Radiation Environment, ed. Q. Hu et al. (Melville, NY: AIP), 222

McComas, D. J., Alexashov, D., Bzowski, M., et al. 2012a, Sci, 336, 1291
McComas, D. J., Allegrini, F., Bochsler, P., et al. 2009a, SSRv, 146, 11
McComas, D. J., Allegrini, F., Bochsler, P., et al. 2009b, Sci, 326, 959
McComas, D. J., Bzowski, M., Frisch, P., et al. 2010, JGRA, 115, A09113
McComas, D. J., Dayeh, M. A., Allegrini, F., et al. 2012b, ApJS, 203, 1
McComas, D. J., Lewis, W. S., & Schwadron, N. A. 2014, RvGeo, doi:10.1002/2013RG000438
Möbius, E., Bochsler, P., Bzowski, M., et al. 2009, Sci, 326, 969
Möbius, E., Bochsler, P., Bzowski, M., et al. 2012, ApJS, 198, 11
Möbius, E., Liu, K., Funsten, H., Gary, S. P., & Winske, D. 2013, ApJ, 766, 129
Reisenfeld, D. B., Allegrini, F., Bzowski, M., et al. 2012, ApJ, 74, 110
Richardson, J. D., Kasper, J. C., Wang, C., Belcher, J. W., & Lazarus, A. J. 2008, Natur, 454, 63
Richardson, J. D., & Wang, C. 2011, ApJL, 734, L21
Roelof, E. 1987, GeoRL, 14, 652
Saul, L., Wurz, P., Rodriguez, D., et al. 2012, ApJS, 198, 14
Schwadron, N. A., Bzowski, M., Crew, G. B., et al. 2009, Sci, 326, 966
Schwadron, N. A., & McComas, D. J. 2013, ApJ, 764, 92
Siewert, M., Fahr, H.-J., McComas, D. J., & Schwadron, N. A. 2012, A&A, 539, A75
Sokół, J. M., Bzowski, M., Tokumaru, M., Fujiki, K., & McComas, D. J. 2013, SoPh, 285, 167
Stone, E. C., Cummings, A. C., McDonald, F. B., et al. 2013, Sci, 341, 150
Wood, B. E., & Izmodenov, V. V. 2010, in AIP Conf. Proc. 1302, Pickup Ions throughout the Heliosphere and Beyond, ed. J. Roux et al. (Melville, NY: AIP), 18
Wood, B. E., Izmodenov, V. V., Linsky, J. L., & Malama, Y. G. 2007, ApJ, 657, 609
Wurz, P., Scheer, J., Saul, L., et al. 2009, SSRv, 146, 173
Zank, G. P., Heerikhuisen, J., Pogorelov, N. V., Burrows, R., & McComas, D. 2010, ApJ, 708, 1092